# Radiative Transfer in Mountains: Application to the Tibetan Plateau

K. N. Liou, Wei-Liang Lee, and Alex Hall

Department of Atmospheric and Oceanic Sciences and
Joint Institute for Regional Earth System Science and Engineering
University of California, Los Angeles, CA 90095

(Accepted for publication in Geophysical Research Letters, October 22, 2007)

**Abstract**

We developed a 3D Monte Carlo photon tracing program for the transfer of radiation in inhomogeneous and irregular terrain to calculate broadband solar and thermal infrared fluxes. We selected an area of 100×100 $km^2$ in the Tibetan Plateau centered at Lhasa city and used the albedo and surface temperature from MODIS/Terra for this study. We showed that anomalies of surface solar fluxes with reference to a flat surface can be as large as 600 $W/m^2$, depending on time of day, mountain configuration, and albedo. Surface temperature is the dominating factor in determining anomalies of the surface infrared flux distribution relative to a flat surface with values as high as 70 $W/m^2$ at cold mountain surfaces. The average surface solar flux over regional domains of 100×100 $km^2$ and 50×50 $km^2$ comprising intense topography can deviate from the smoothed surface conventionally assumed in climate models and GCMs by 10-50 $W/m^2$.

## 1. Introduction

The energy emitted by the sun that is available at the top of the Earth's atmosphere (TOA) is a function of three sets of factors that include latitude, solar hour angle, and the Earth's position relative to the sun and can be precisely calculated [*Liou*, 2002]. The solar flux received by the surface involves the attenuation of solar beam by scattering and absorption caused by atmospheric gases, aerosols, and cloud particles. The last comprises terrain characteristics including elevation, slope, orientation, and surface albedo. In mountainous terrain, the direct and diffuse solar fluxes reaching a sloping surface can be reflected to space and/or to other surfaces that cannot be fully accounted for by the conventional plane-parallel radiative transfer approach for a flat surface. For low solar elevation angles, the curvature of the Earth can also pose limitations on the use of the conventional plane-parallel radiative transfer approach for atmospheric calculations, but this issue is secondary compared to intense topographic effects. The problem of radiative transfer in mountains is three-dimensional in nature and it is indeed intricate. Evaluation of the solar flux available at mountain surfaces by means of an accurate analytic solution with appropriate boundary conditions imposed appears to be very difficult, if not impossible.

Nevertheless, a variety of models of varying sophistication and complexity have been developed to compute solar flux components in rugged terrain [*e.g., Duguay, 1993*]. The direct incident beam is generally computed by introducing a cosine correction of the local zenith angle and considering the shadow caused by topography [*e.g., Olyphant*, 1986]. Diffuse radiation has been modeled as being proportional to the area of sky dome visible to the target surface [*e.g., Dozier and Frew*, 1990]. Factors contributing to terrain-reflected flux, particularly significant over snow surfaces [*Dozier*, 1980], have generally not been considered explicitly, but are approximated by assuming a first-order reflection between surrounding terrain and the target surface. *Miesch et al*. [1999] used a Monte Carlo approach to compute the radiance reaching the satellite-borne sensor over a simple 2D rugged terrain to demonstrate its importance in remote sensing application. Moreover, *Chen et al*. [2006] developed a 3D Monte Carlo radiative transfer model that calculates solar flux components exactly given a realistic distribution of scatterers and absorbers in the atmosphere and provided the first definitive assessment of the relative importance of the flux components in a clear-sky atmosphere.

It is clear that significant progress has been made on the understanding and quantification of solar flux transfer in intense topography. However, the thermal infrared (IR) radiation emitted from mountains with an inhomogeneous surface temperature distribution has not been studied to understand its significance in surface energy balance. IR radiative transfer involving mountainous surfaces depends on their temperatures, which are related to elevation, and the amount of absorbing and emitting gases above. At the same time, emissions and reflections between nonblack mountains can also take place. To the best of our understanding thermal IR radiative transfer in mountains remains an uncharted research subject.

We investigate the effect of mountains on the transfer of broadband solar and thermal infrared fluxes and attempt to understand the underlying physical processes. For the transfer of solar radiation, we follow the Monte Carlo approach developed by *Chen et al.* [2006] to trace photons emitted by the sun, a point source, and evaluate their interactions with the atmospheres (without clouds) and the underlying mountains with known

topography and albedo. Moreover, we develop an innovative Monte Carlo approach involving the transfer of emitted thermal IR radiation from mountains and its interactions with the absorbing and emitting atmosphere above. These are discussed in Section 2. In Section 3, we apply the 3D solar and thermal IR radiative transfer to the Tibetan Plateau and use the snow and albedo data available from MODIS to conduct surface radiation analysis. Conclusions are given in Section 4.

## 2. Spectral 3D Radiative Transfer in Mountains

The Monte Carlo method appears to be the best approach for the intricate radiative transfer problem involving complex 3D topography because photons can be traced exactly in any irregular and inhomogeneous space configuration. In the present Monte Carlo approach, the domain of study in the atmosphere is discretized in terms of finite cubic cells such that each can undergo absorption, scattering, and emission. Photons entering TOA are defined by unit irradiance and its direction is determined by the sun's position. The optical path length $l$, which a photon travels from TOA to the first encounter with an air molecule or between two encounters, is determined by Beer's law: $l = -\ln \xi$, where $\xi$ is a random number uniformly distributed within the interval [0,1]. When the photon reaches the point of encounter, the probability of its being absorbed or scattered is dependent on the single-scattering albedo. In the complete absorption case, this photon is terminated. But if scattering occurs, then the photon is deflected to the direction determined by the particle's scattering phase function, a function of incoming and outgoing directions characterized by $\mu$ (cosine of the zenith angle, $\theta$) and $\varphi$, the azimuthal angle. Once the photon hits the ground, the probability of its being reflected is given by the surface albedo assumed to be Lambertian for flux calculations and the direction of the reflected photon is determined by $\mu = \cos\theta = \sqrt{\xi_1}$ and $\varphi = 2\pi\xi_2$, where $\xi_1$ and $\xi_2$ are random numbers within the interval [0,1]. Each photon is traced until it is absorbed by the atmosphere or leaves TOA. The flux at each cell facet can be obtained by tallying the total weight of the photons crossing the cell's boundary.

The same procedure is followed for the photon tracing process involving thermal IR transport, except that photons are emitted from the atmosphere and mountain surfaces. For computational purposes, these surfaces are discretized by cubic cells matching those of the atmosphere's lower boundary. For an infinitesimally small cell, emission must be isotropic so that the emitted flux from one side of the cubic cell for a given wavelength $\lambda$ can be written as

$$F_\lambda(i, j, k) = \pi\varepsilon_\lambda(i, j, k)B_\lambda(T(i, j, k)), \tag{1}$$

where $\varepsilon_\lambda$ and $T$ are, respectively, emissivity and temperature of the cubic cell defined by the 3D position denoted by ($i$, $j$, $k$) and $B_\lambda$ is the Planck function. The total monochromatic flux emitted from the whole domain is then

$$F_{\lambda,\text{total}} = \sum_i \sum_j \sum_k \delta_c F_\lambda(i, j, k). \tag{2}$$

For atmospheric cells, $\delta_c$ is equal to 6 accounting for emission from six facets of the cubic cell. For land cells, since only the sides adjacent to the atmosphere emit photons, $\delta_c$ can be an integer between 0 and 5 to be determined by topography. The number of photons emitted from a facet is proportional to the ratio of the flux emitted from the facet with respect to the total flux in the domain.

In clear sky, the effect of scattering in the atmosphere is negligible in thermal IR so that the only factor that determines the effective optical depth is absorption. It follows that the emissivity of atmospheric cubic cells can be parameterized in terms of optical depth [*Chen and Liou*, 2006]. In the Monte Carlo simulation, if $M$ photons enter a cubic cell and undergo absorption, then the absorptivity of the cell is given by $A = 1 - N/M$, where $N$ is the number of photons escaped from the cell after stochastic tracking described above. Under thermodynamic equilibrium, emissivity $\varepsilon$ equals absorptivity $A$. We have used a number of atmospheric cubic cells (e.g., $1\times1\times1$ km$^3$ and $0.1\times0.1\times0.1$ km$^3$) to test computational accuracy and found that the flux results from these two models differ only in five decimal points. A large number of photons ($10^9$-$10^{11}$) have been used in various computations to avoid truncation error and to achieve accurate statistics.

We followed the correlated k-distribution approach for effective incorporation of line absorption in the 3D Monte Carlo photon tracing program covering the entire solar and thermal IR spectra. The absorbing gases included in broadband calculations are $H_2O$, $CO_2$, $O_3$, $O_2$, $CH_4$, $N_2O$, CFCs, CO, $O_2O_2$, $O_2N_2$, and $NO_2$ [*Gu et al.,* 2006]. The solar spectrum (0.2-5 μm) was divided into 6 bands, while the thermal infrared spectrum (0-2200 cm$^{-1}$) were grouped into 12 bands in accordance with the position of gaseous absorption [*Fu and Liou*, 1992]. Contributions of Rayleigh scattering and background aerosols were also included in Monte Carlo calculations.

## 3. Broadband Flux Transfer in Mountains Applied to the Tibetan Plateau

The Tibetan Plateau, which covers about 2.4 million km$^2$ with an average height of 4.7 km, has a profound influence on the general circulation of the atmosphere due to its uplift of large scale flow patterns and its insertion of heating with a confining lower boundary at high levels. The wintertime dynamic effect enhances the southward transport of the Siberian high and leads to a large trough in the jet stream extending into the Pacific. The summertime elevated heat source has been recognized by a number of meteorologists [*Ye et al*., 1979] in conjunction with the formation and maintenance of the Asian summer monsoon, the onset of Meiyu, the East Asian summer monsoon rainfall period, and the summertime heavy rainfall frequently occurring in central China. Knowledge of the Tibetan Plateau heating and its interactions with the complex regional dynamics and the consequent effects has remained rather limited. Problems associated with the vertical profile of radiative heating rates over the mountainous region, the coupling of the surface to the lower atmosphere through boundary layer convection, and the snow-albedo feedback in regional and global climate change appear to be largely unresolved and often ignored.

To demonstrate the importance of intense topography on surface radiative fluxes, we selected a domain size of 100 by 100 km centered at Lhasa city in this study (note that the same analysis can be applied to other regions as well). The average height for this domain is about 4.37 km. Surface topography with a 1 km resolution was taken from the HYDRO1k geographic database available from the U. S. Geological Survey's National Center for Earth Resources Observation and Science data center. For solar radiative transfer calculations, we used a horizontal resolution of $1\times1$ km$^2$ with 29 vertical layers from surface to 70 km. For thermal IR calculations, we employed a grid cell size of $0.5\times0.5$ km$^2$ and assigned $200\times200\times20$ homogeneous cubic cells for the domain of study. Inputs to the 3D radiative transfer calculations include albedo and surface temperature

taken from the MODIS aboard the Terra satellite at a 0.05 degree (~ 5 km) resolution. The MODIS temperature data was 8-day composite from 03/14/2001 to 03/21/2001, the spring equinox, while the corresponding albedo data was 16-day composite from 03/06/2001 to 03/21/2001. MODIS albedo dataset consists of a broadband value covering the entire solar spectrum and two spectral albedos in the VIS (0.3-0.7 μm) and near IR (0.7-5.0 μm). Snow and bare land surfaces would have different spectral emissivities but for the purpose of studying mountain effects, a value of 0.95 was assumed. Temperature and water vapor profiles were taken from the ECMWF reanalysis data with a 1º (~ 100 km) resolution corresponding to the same time period as surface temperature. Thus, only one atmospheric profile was used in radiative transfer analysis. Because the lowest level in the reanalysis data is 4.5 km, we extended the vertical temperature and water vapor profiles to mountainous surfaces by extrapolation. Lastly, the ozone and other trace gaseous profiles corresponding to the standard midlatitude atmosphere were used in the following calculations.

Figure 1 shows the maps of surface elevation, snow cover, broadband albedo, and daytime surface temperature. The pixels with elevation lower than 2.75 km are along the beds of the Lhasa and Yarlung Tsangpo rivers denoted by blue lines. The highest elevation in this area is about 6 km. Also, the yellow color indicates the position of valley. The largest snow cover, generally associated with high elevation, resides at the northwest corner of the domain. *Pu et al.* [2007] compared the snow cover over the Tibetan Plateau determined from MODIS to the in-situ station snow data and showed that the overall accuracy of satellite-derived snow data is about 90 %. In terms of albedo, the high elevation areas and the north side of mountainous regions depict values greater than 0.5 associated with snow cover. Albedo is generally less than 0.2 along the valley areas. Surface temperature correlates well with elevation with high values (red colors) along the rivers and valley basins.

The upper panels in Figure 2 display the spatial distribution of anomalies (or deviations) of the surface net solar flux on mountains from a flat surface (4.37 km with an average albedo of 0.22). The net solar radiative flux is defined as the difference of the downward and upward fluxes. The left panel results are for 1 hour after sunrise corresponding to a solar zenith angle of 77º. Clearly displayed are strong positive anomalies on the order of 200 W/m$^2$ at the east side of mountains facing the sun, and negative anomalies of ~ -150 W/m$^2$ at the west side (shaded areas). Also shown are small pockets of strong negative anomalies (~ -100 W/m$^2$) scattered at the sunny side of the figure due to high albedo in this region. The right panel results correspond to the case of spring equinox at noon with a solar zenith angle of 29°. Flux anomalies are larger in comparison to the sunrise case because of the stronger incident solar insolation during noon. They are also more concentrated in areas of steep topography because of lower solar zenith angle. Positive and negative anomalies located at the south and north sides of the domain can be as large as 500 and -300 W/m$^2$, respectively. At high albedo areas, strong negative anomalies of ~-400 W/m$^2$ are also found. Substantial surface solar flux differences between the two cases are clearly displayed. We also conducted an experiment to examine the effect of utilizing two MODIS spectral albedo values on surface net flux calculations. Mean and standard deviation differences between one- and two- albedo cases are -0.20 and 4.99 W/m$^2$, respectively, for one hour after sunrise, and -0.57 and 11.66 W/m$^2$ for the noon condition. These values are small as compared to large

anomalies on the order of 100 W/m$^2$ between mountains and a flat surface.

The lower panels of Figure 2 illustrate the spatial distributions of the mountain surface net IR flux anomalies during daytime (10.30 am) and nighttime (10.30 pm). The net IR radiative flux is defined as the difference of the upward and downward fluxes. The surface temperature of the flat surface is the average temperature of the mountain surface in the domain: 288 K for daytime and 264 K for nighttime. The pattern of net IR flux closely follows that of surface temperature distribution, the most dominant factor in the IR radiative balance over mountains. Negative anomalies of ~-40 W/m$^2$ occur over warmer surfaces at lower elevation, whereas positive anomalies can reach 70 W/m$^2$ at high elevation with cold temperatures. To a lessen degree the amounts of absorbing and emitting gases above the two types of surfaces also contribute to these anomalies.

Finally, we investigate differences of the domain-averaged net radiative flux on mountains and a flat surface as a function of time of day using two surface albedos of 0.2 and 0.7 for the whole domain, as shown in Fig. 3 where two different scales were used. Two surface domains of 50×50 km$^2$ (centered at Lhasa) and 100×100 km$^2$ were employed for illustration purposes. For solar radiation, the mountain area generally receives less flux than the flat surface counterpart due in part to additional reflections to the atmosphere produced by rugged mountains and also to different atmospheric conditions above. Difference can be as large as 50 W/m$^2$ at 1 hour before sunrise for a surface albedo of 0.2. For a snow-like surface albedo of 0.7, differences on the order of 40 W/m$^2$ between the mountain and flat surface cases are consistent throughout the day because of the greater reflecting power. In thermal IR radiation calculations, the daytime surface temperatures used correspond to 12.00 and 18.00 local times, while for nighttime, they correspond to 6.00 and 24.00 local times. The net IR fluxes are generally larger on mountain surfaces than on a flat surface due to the coupled emission contributions from mountains. However, differences are small, only about 1.5 W/m$^2$ at local noon, and 0.5 W/m$^2$ at other times. Lastly, we note from Fig. 3 that flux differences between the two assumed domains are relatively small, but in general these differences should be determined by terrain complexity and irregularity within the domain.

In this short paper, we have not addressed a separate and diverse issue concerning the radiative significance of inhomogeneous and irregular terrain on satellite remote sensing of the atmosphere and the surface in which intensity, not flux, is the measured parameter. Surface bidirectional reflection information becomes critical to interpretation and understanding of TOA intensity patterns over a mountain domain, an intricate remote sensing issue requiring in-depth radiative transfer analysis.

## 4. Conclusions

A 3D Monte Carlo photon tracing program has been developed for the transfer of radiation in inhomogeneous and irregular terrain to evaluate broadband solar and thermal IR fluxes at mountain surfaces. In numerical computations, the atmosphere and mountain surfaces are discretized in cubic cells the sizes of which are sufficiently small that their solar single-scattering properties are homogeneous, while the IR emissivities and absorptivities are uniform and isotropic as to achieve thermodynamic equilibrium. Radiation contributions from clouds and/or heavy aerosol loading can be incorporated in this 3D radiative transfer program, although computational efforts would be substantially increased, making this a subject for future investigation. We selected a 100×100 km$^2$ part

of the Tibetan Plateau centered at Lhasa city with a horizontal resolution of 1 $km^2$ for this study.

We used the surface flux anomalies between mountain surfaces and the corresponding flat surface with an averaged height typically assumed in climate models to examine the significance of two results. For solar radiation, surface flux anomalies in clear sky can be as big as 600 $W/m^2$, depending primarily on time of day, mountain configuration, surface albedo, and to a lessen degree the atmospheric absorption and scattering above. Surface temperature is the dominating factor in controlling anomalies of the surface IR flux distribution and they can be as high as 70 $W/m^2$ at cold mountain surfaces. The subgrid variability for both solar and thermal IR surface fluxes is indeed large and significant with respect to other land surface processes. The domain-averaged surface fluxes over two mountain areas of 100×100 $km^2$ and 50×50 $km^2$ are subsequently studied and compared to those computed from an averaged height with a flat surface. For an albedo of 0.2, differences range from 10 to 50 $W/m^2$ depending on time of day. But for a large albedo of 0.7, a consistent difference of about 40 $W/m^2$ is shown. Differences for thermal IR surface fluxes between the mountain and flat configurations are only on the order of 1 $W/m^2$.

In summary, we demonstrated that mountain effects on surface radiative balance are substantial in terms of subgrid variability as well as domain average conditions. A significant solar flux deviation of about 10-50 $W/m^2$ from the smoothed topography of conventional GCMs and climate models would occur if realistic mountain features were not accounted for in the modeling of surface energy balance. Because of the computational burden in 3D Monte Carlo photon tracing program, it is necessary to develop parameterization for the most essential radiation components for effective incorporation in climate models. This is a challenging task, but it must be accomplished if we wish to build a physically-based surface energy balance model for climate simulation in areas of intense topography.

**Acknowledgements**. The research of this work has been supported by NSF Grants ATM-0331550 and ATM-0135136, and DOE Grant DE-FG03-00ER62904.

**References**

Chen, Y., and K. N. Liou (2006), A Monte Carlo method for 3D thermal infrared radiative transfer, *J. Quant. Spectrosc. Radiat. Transfer*, 101, 166-178.

Chen, Y., A. Hall, and K. N. Liou (2006), Application of 3D solar radiative transfer to mountains, *J. Geophys. Res.,* 111, D21111,doi:10.1029/2006JD007163.

Dozier, J. (1980), A clear-sky spectral solar radiation model for snow-covered mountainous terrain, *Water Resour. Res.*, 16, 709-718.

Dozier, J., and J. Frew (1990), Rapid calculations of terrain parameters for radiation modeling from digital elevation data, *IEEE Trans. Geosci. Remote Sens.,* 28, 963-969.

Duguay, C. (1993), Radiation modeling in mountainous terrain: Review and status, *Mt. Res. and Dev.*, 13, 339–357.

Fu, Q., and K. N. Liou (1992), On the correlated k-distribution method for radiative transfer in nonhomogeneous atmospheres, *J. Atmos. Sci*., **49**, 2139-2156.

Gu, Y., K. N. Liou, Y. Xue, C. R. Mechoso, W. Li, and Y. Luo (2006), Climatic effects of different aerosol type in China simulated by the UCLA AGCM, *J. Geophys. Res.,* 111, D15201,doi:10.1029/2005JD006312.

Liou, K. N. (2002), *An Introduction to Atmospheric Radiation*, 2nd ed., Academic Press, 583 pp., Academic Press, San Diego.

Miesch, C., X. Briottet, Y. H. Herr, and F. Cabot (1999), Monte Carlo approach for solving the radiative transfer equation over mountainous and heterogeneous areas, *Appl. Opt.*, 38, 7419–7430.

Olyphant, G. A. (1986), The components of incoming radiation within a mid-latitude alpine watershed during the snowmelt season, *Arct. Alp. Res.*, 18, 163-169.

Pu, Z., L. Xu, and V., Salomonson, (2007), MODIS/Terra observed seasonal variations of snow cover over the Tibetan Plateau, *Geophys. Res. Lett*., 34, L06706, doi:10.1029/2007GL029262.

Ye, D. (Yeh, T. C.) (1979), *The Meteorology of Qinghai-Xizang Plateau*, edited by D. Ye and Y. X. Gao, Chap.1. Science Press, Beijing (in Chinese).

**Figure Captions**

Figure 1. Maps of the surface elevation, snow cover, albedo, and daytime surface temperature. Surface topography was taken from the HYDRO1k geographic database with a 1 $km^2$ resolution, while the snow cover, albedo, and surface temperature were from MODIS at a 0.05 degree (~ 5 km) resolution.

Figure 2. The upper panels display the spatial distribution of deviations of the surface net solar flux, defined as difference of the downward and upward fluxes, on mountains from a flat surface (4.37 km with an average albedo of 0.22). The lower panels illustrate the spatial distribution of deviations of the surface net IR flux, defined as difference of the upward and downward fluxes, on mountains from this flat surface during daytime (10.30 am) and nighttime (10.30 pm).

Figure 3. Differences of the domain-averaged net radiative flux on mountains and a flat surface as a function of time of day using surface albedos of 0.2 and 0.7 for two domains of 50×50 $km^2$ (centered at Lhasa) and 100×100 $km^2$.

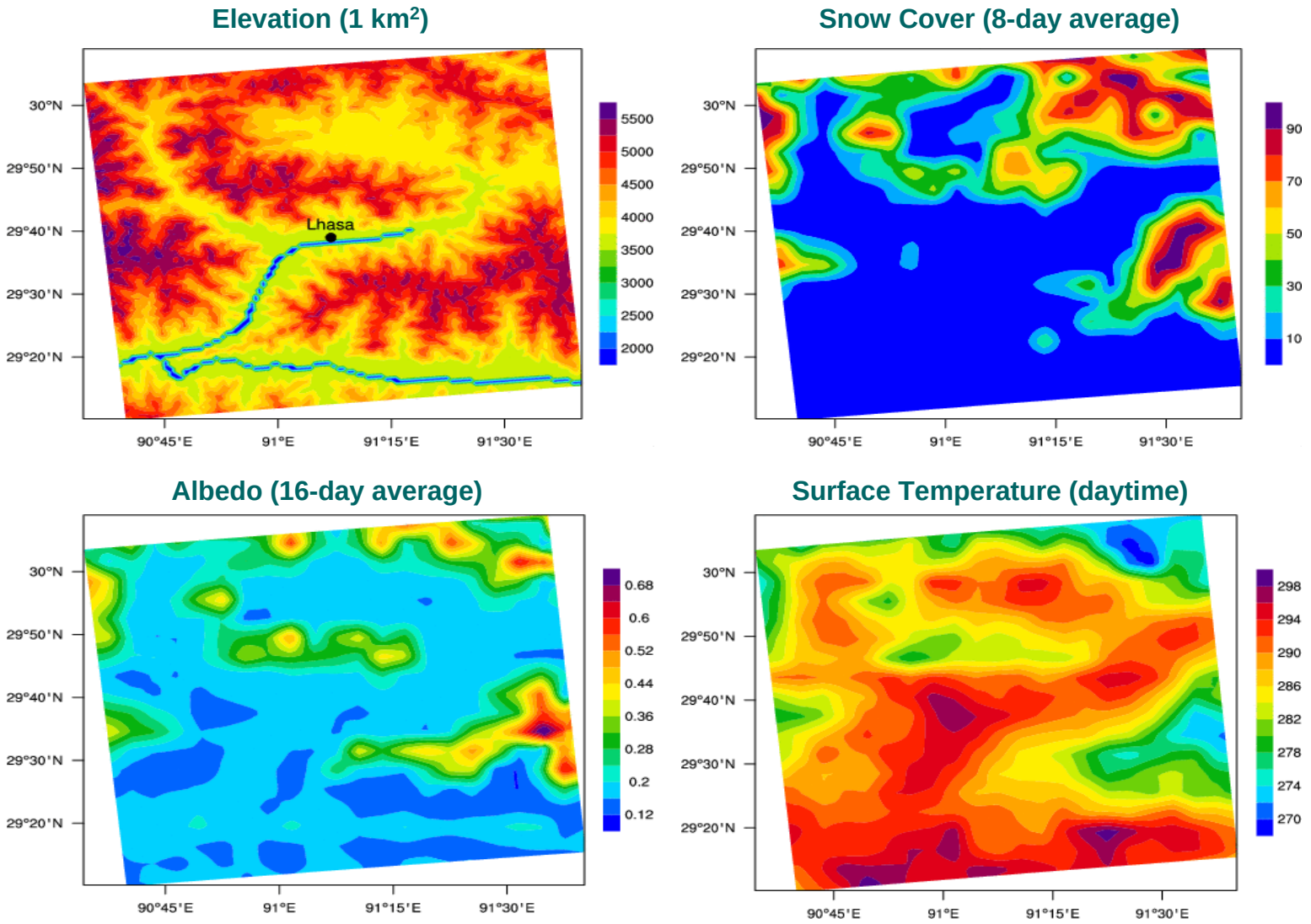


Figure 1. Maps of the surface elevation, snow cover, albedo, and daytime surface temperature. Surface topography was taken from the HYDRO1k geographic database with a 1 km$^2$ resolution, while the snow cover, albedo, and surface temperature were from MODIS at a 0.05 degree (~ 5 km) resolution.

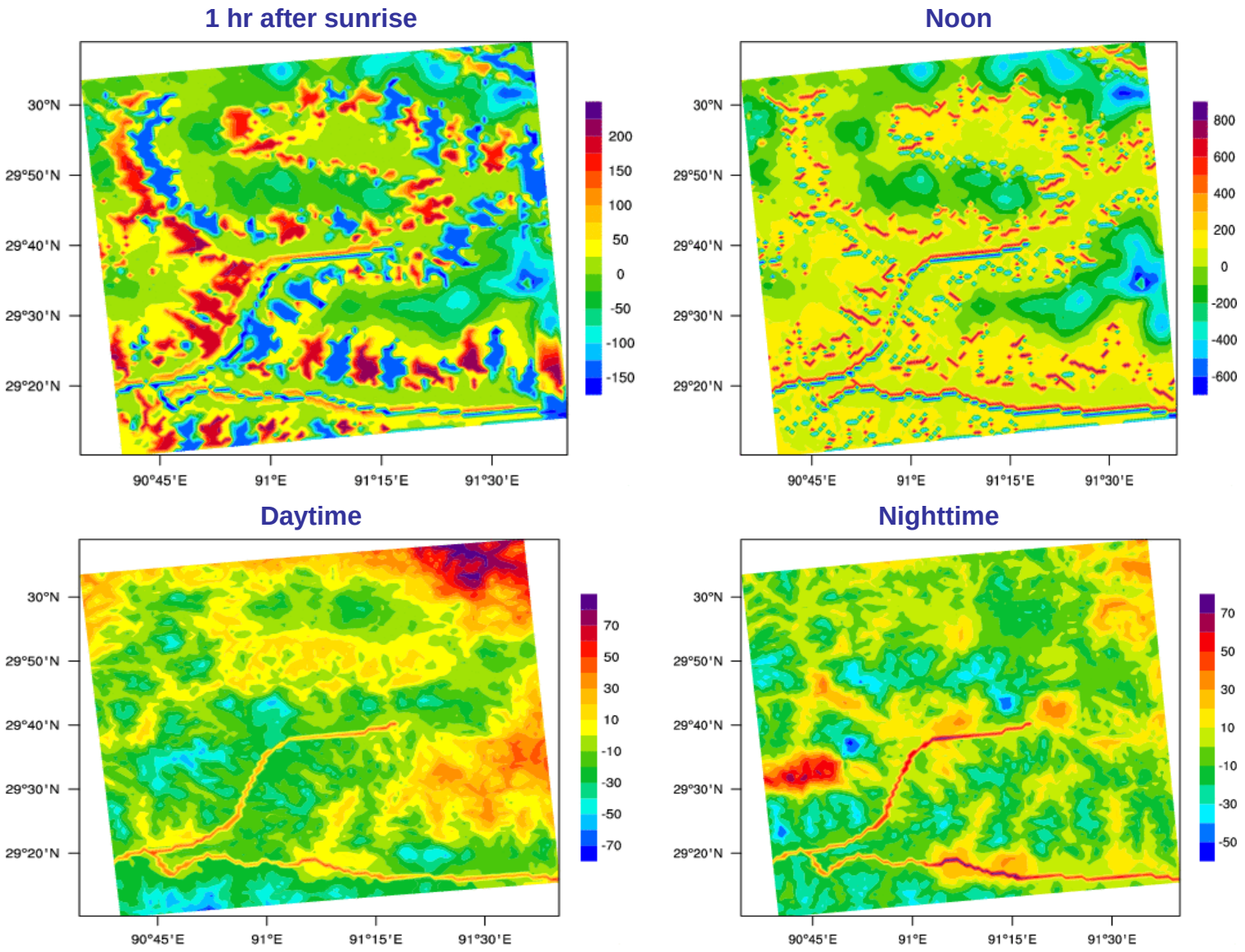


Figure 2. The upper panels display the spatial distribution of deviations of the surface net solar flux, defined as difference of the downward and upward fluxes, on mountains from a flat surface (4.37 km with an average albedo of 0.22). The lower panels illustrate the spatial distribution of deviations of the surface net IR flux, defined as difference of the upward and downward fluxes, on mountains from this flat surface during daytime (10.30 am) and nighttime (10.30 pm).

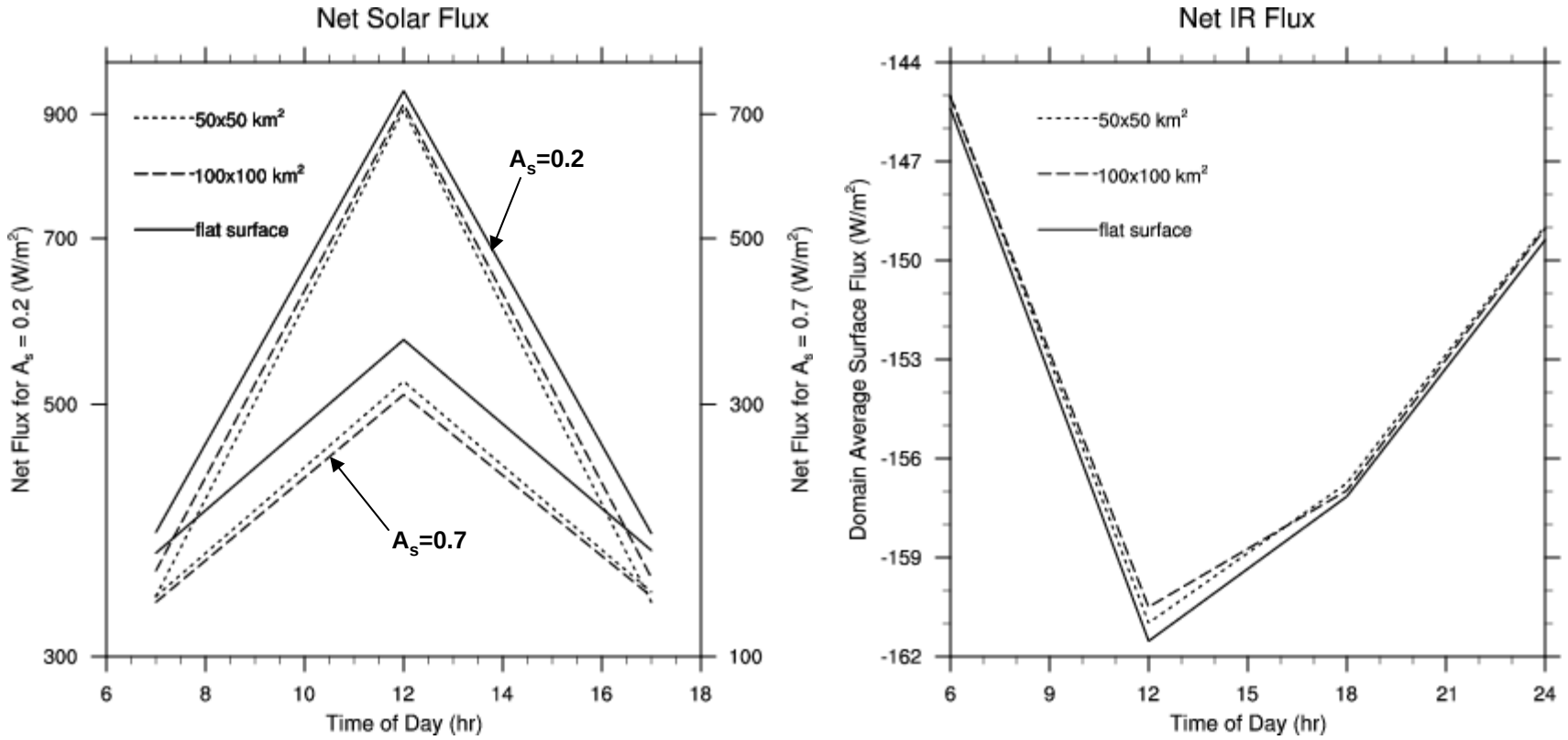


Figure 3. Differences of the domain-averaged net radiative flux on mountains and a flat surface as a function of time of day using surface albedos of 0.2 and 0.7 for two domains of 50×50 km$^2$ (centered at Lhasa) and 100×100 km$^2$.